Acoustic scattering from double-diffusive microstructure

Andone C. Lavery[a)]
Department of Applied Ocean Physics and Engineering, Woods Hole Oceanographic Institution, Woods Hole, Massachusetts 02543

Tetjana Ross
Department of Oceanography, Dalhousie University, Halifax, Nova Scotia B3H 4J1, Canada

Laboratory measurements of high-frequency broadband acoustic backscattering (200–600 kHz) from the diffusive regime of double-diffusive microstructure have been performed. This type of microstructure, which was characterized using direct microstructure and optical shadowgraph techniques, is identified by sharp density and sound speed interfaces separating well-mixed layers. Vertical acoustic backscattering measurements were performed for a range of physical parameters controlling the double-diffusive microstructure. The echoes have been analyzed in both the frequency domain, providing information on the spectral response of the scattering, and in the time domain, using pulse compression techniques. High levels of variability were observed, associated with interface oscillations and turbulent plumes, with many echoes showing significant spectral structure. Acoustic estimates of interface thickness (1–3 cm), obtained for the echoes with exactly two peaks in the compressed pulse output, were in good agreement with estimates based on direct microstructure and optical shadowgraph measurements. Predictions based on a one-dimensional weak-scattering model that includes the actual density and sound speed profiles agree reasonably with the measured scattering. A remote-sensing tool for mapping oceanic microstructure, such as high-frequency broadband acoustic scattering, could lead to a better understanding of the extent and evolution of double-diffusive layering, and to the importance of double diffusion to oceanic mixing. © *2007 Acoustical Society of America.* [DOI: 10.1121/1.2764475]

I. INTRODUCTION

Acoustic scattering techniques make it possible to rapidly characterize oceanic microstructure and fine structure at high-resolution and on temporal and spatial scales difficult to achieve using traditional oceanographic profiling instruments. Even without a detailed understanding of the scattering physics, acoustic scattering techniques have provided high-resolution, synoptic images of physical processes occurring in the ocean interior, e.g., internal waves (Proni and Apel, 1975; Moum *et al.*, 2003), hydraulic jumps (Farmer and Armi, 1999), and oceanic thermohaline fine structure across oceanographic fronts (Holbrook *et al.*, 2003). There is the potential to obtain additional information regarding oceanic microstructure and fine structure by developing a deeper understanding of the underlying scattering processes, though confounding effects due to other sources of scattering, such as zooplankton, need to be considered (Lavery *et al.*, 2007). For example, the dissipation rate of turbulent kinetic energy has been inferred from high-frequency acoustic scattering measurements in regions of elevated turbulent microstructure (Warren *et al.*, 2003).

Microstructure, which can be broadly categorized into turbulent and double-diffusive microstructure, refers to any physical process that gives rise to small-scale temperature and salinity fluctuations, resulting in density and sound speed fluctuations, which can scatter sound. There are two types of double-diffusive microstructure (Schmitt, 1994): the diffusive regime, which occurs when temperature and salinity generally increase with increasing depth, and the salt fingers regime, which occurs when temperature and salinity generally decrease with increasing depth. In this study we concentrate on double-diffusive interfaces generated by the diffusive regime of double-diffusive microstructure. Double-diffusive microstructure is maintained since the molecular diffusion of heat is two orders of magnitude faster than the molecular diffusion of salt. For the diffusive regime of double-diffusive microstructure, salinity and temperature gradients have opposing influences on the density, with the salinity gradient acting to stabilize the density and the temperature gradient acting to destabilize the density. Rapid heat transfer (relative to salt) causes small vertical perturbations to be suppressed and results in sharp interfaces separating well-mixed layers (Fig. 1). High-latitude regions (Neal *et al.*, 1969; Muench *et al.*, 1990) are generally susceptible to this type of microstructure, which is manifested as thermohaline staircases with a series of well-mixed layers separated by relatively thin interfaces.

There have been few studies pertaining to high-frequency acoustic scattering from either salt fingers or the diffusive regime of double diffusion. A theoretical study of the influence of salt finger thermohaline structure on acoustic propagation was performed by Mellberg and colleagues (Mellberg and Johannessen, 1972; Mellberg *et al.*, 1974) using ray-tracing techniques, though no subsequent measure-

---
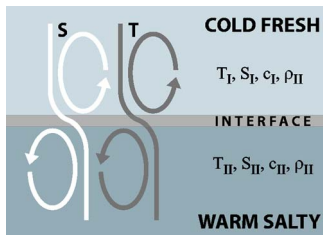
a)Electronic mail: alavery@whoi.edu

FIG. 1. (Color online) Illustration of the diffusive regime of double diffusion.

ments were performed. In contrast to double-diffusive microstructure, there have been a number of theoretical studies (Goodman, 1990; Seim, 1999; Lavery *et al.*, 2003) and band-limited field measurements (Seim *et al.*, 1995; Ross and Lueck, 2003; Warren *et al.*, 2003) of scattering from turbulent microstructure, and a series of laboratory measurements focusing on turbulent temperature microstructure (Goodman *et al.*, 1992; Stanton *et al.*, 1994; Oeschger and Goodman, 1996, 2003). A recent review (Kelley *et al.*, 2003) suggests that there are fundamental questions regarding the formation and evolution of double-diffusive microstructure, for example, the importance of layer splitting in controlling layer thickness, that would benefit from a rapid, high-resolution, remote mapping technique such as high-frequency acoustic scattering.

In order to improve our understanding of scattering from oceanic microstructure, controlled laboratory measurements of high-frequency broadband acoustic scattering from single, sharp, double-diffusive interfaces have been performed over a range of parameters controlling the double-diffusive microstructure. The experimental methods are described in Sec. II. The echoes from the double-diffusive interfaces have been analyzed in both the spectral domain (Sec. II F 1), as the spectral characteristics of the echoes provide one approach for discrimination between, and identification of, different types of microstructure, and the temporal domain (Sec. II F 2), using pulse compression techniques (Chu and Stanton, 1998) that allow individual scattering features to be resolved, such as the front and back edges of the double-diffusive interfaces. The ping-to-ping characteristics (Sec. III A), variability (Sec. III B), and coherence (Sec. III C) of the echoes are analyzed, and the dominant physical factors influencing the scattering are identified (Sec. III D). The interface thickness has been inferred acoustically (Sec. III E) and compared to measurements based on direct microstructure and optical shadowgraph techniques. A simple one-dimensional weak-scattering scattering model based on actual density and sound speed profiles has been developed (Sec. IV). The results are summarized in Sec. V.

II. EXPERIMENTAL SETUP, METHODS, AND PROCEDURES

The measurements of high-frequency broadband acoustic scattering from double-diffusive (DD) interfaces were conducted at a tank facility (Schmitt *et al.*, 2005) at the Woods Hole Oceanographic Institution (WHOI). Direct measurements of the physical properties of the DD interface were also performed. The relevant details of this facility and

the instrumentation used to perform the measurements are described below. The experiments were performed a total of six times. The results presented here correspond to the experiment performed between 27 July (year day 208) and 10 August (year day 222) 2004 and are representative of the results obtained in the other experiments at the WHOI facility.

A. Double-diffusive interface tank

The double-diffusive interface tank was cylindrical in shape, 4.7 m deep, 91.4 cm in outer diameter, and with 2.54 cm thick walls (Fig. 2). The top of the tank was surrounded by a platform from which the acoustic and microstructure instruments were deployed. The bottom of the tank was heated by a resistive heating element powered by a variable transformer and controlled by a thermostat. The top of the tank was cooled by means of a heat exchanger consisting of coiled copper tubing mounted beneath foam that provided both floatation and insulation. The side-walls were insulated to minimize heat loss. It was estimated that approximately 30% of the heat supplied to lower layer was lost through the side walls (Schmitt *et al.*, 2005). Temperature differences of 10–15 °C across an interface approximately 1–3 cm thick, corresponding to temperature gradients of 300–1500 °C/m, were maintained for extended periods of time. Initially, the tank was filled to the desired location of the interface (200–230 cm below the top of the tank, co-located with the shadowgraph imaging system) with room-temperature fresh water filtered with a 5-μm filter. Chlorine was used to minimize the growth of biota in the tank. Commercially available "SeaSalt," manufactured by Lake Products Co., was added to set the salinity at approximately 15 psu. The upper layer was then slowly filled with cold fresh filtered water, resulting in initial salinity gradients of 300–1500 psu/m. The slow diffusion of salt reduces the maintainable temperature contrast across the interface, and, after 2–3 weeks, the double-diffusive system overturns and becomes fully mixed (Fig. 3).

B. Physical properties of the upper and lower mixed layers

Two fixed temperature (T) and conductivity (C) sensors (Falmouth Scientific, Inc.), collecting data every 30 s, were mounted within the top and bottom mixed layers at depths of 1 and 3 m. The 1978 Practical Salinity Scale (PSS78) (Fofonoff and Millard, 1983) was used to calculate salinity (S) from measurements of conductivity, temperature, and pressure. Density (ρ) and sound speed (c) were also derived from these measurements (Fofonoff and Millard, 1983). Throughout this study, properties of the upper and lower mixed layers are denoted by the subscripts "I" and "II," respectively (Table I).

The overall stability of the DD interface system is determined by the density ratio $R_\rho = \beta \Delta S / \alpha \Delta T$, where $\alpha = -(1/\rho)\partial\rho/\partial T$ and $\beta = (1/\rho)\partial\rho/\partial S$ are the thermal expansion and haline contraction coefficients, respectively, and $\Delta T = T_{II} - T_I$ and $\Delta S = S_{II} - S_I$ are the temperature and salinity differentials between the upper and lower mixed layers. The heating and cooling of the DD interface tank were approxi-
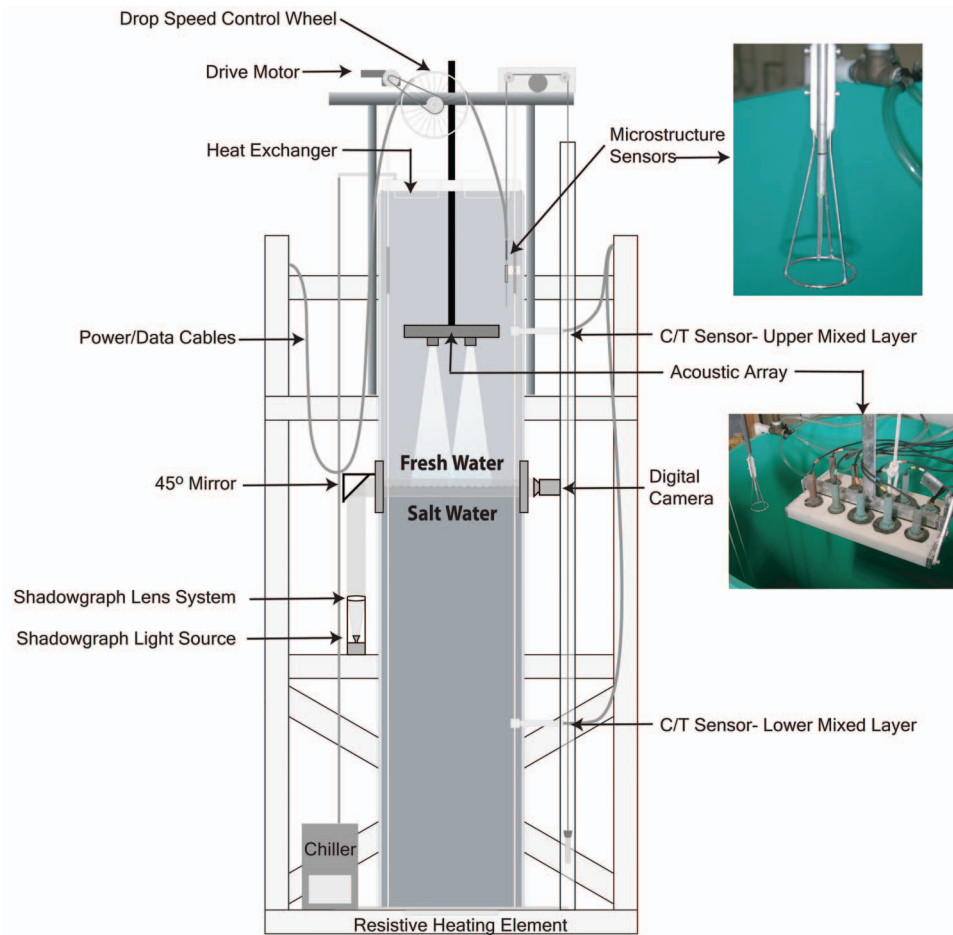
FIG. 2. Illustration of the double-diffusive interface tank.

mately constant throughout the July–August 2004 experiment, so that R_ρ was maintained at values between 4 and 5, except on year days 212 (29 July), and 216 (4 August) when the cooling was removed to maintain the salinity differential during a period of inactivity in the laboratory and to control the density ratio. Removal of the heating and cooling results in a thickening of the interface, which slows the diffusion of salt across the interface. A sharp interface can be reestablished by reapplying the heating and cooling. Towards the end of the experiment, $R_\rho \to 1$, the fluxes across the interface are largest, and the system becomes unstable and ultimately overturns.

C. Direct microstructure measurements

High-resolution microstructure probes (Precision Measurement Engineering, Inc.: Model 125 MicroScale Conductivity and Temperature Instrument), consisting of a fast-response thermistor (FP-07) closely co-located to a four-electrode conductivity cell, were used to directly measure the vertical temperature and conductivity structure across the interface. The fall rate of the sensors was controlled by a geared motor, typically set to 10 cm/s. The microstructure and depth data were digitally recorded at 1 kHz using an 8-bit 16-channel A/D converter (National Instruments Model
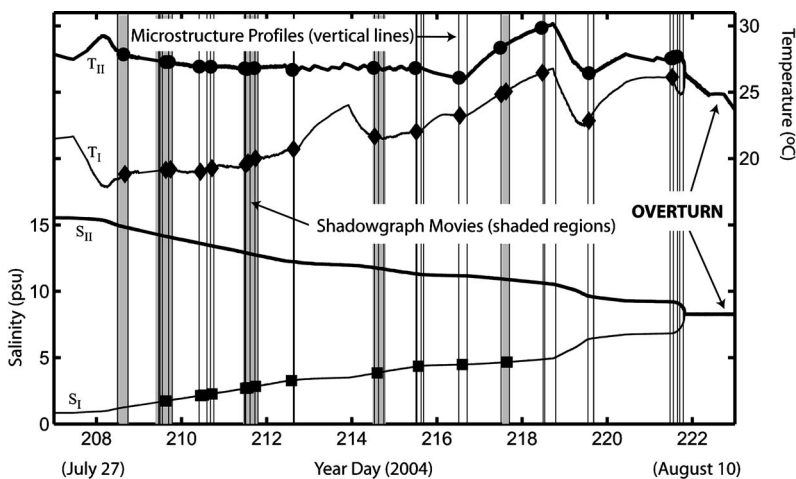

FIG. 3. Temperature and salinity evolution in the upper and lower mixed layers of the DD interface tank during the July–August 2004 experiment. The circles show the times of the 30-min, 1-Hz, 250-kHz BB data acquisition periods, the squares show the times of the 30-min, 1-Hz, 500-kHz BB data acquisition periods, and the diamonds show the times of the 3-min, 10-Hz, 250-kHz BB data acquisition periods. The vertical lines correspond to the times at which direct microstructure measurements were performed. The gray shading corresponds to times at which digital shadowgraph movies were collected.

TABLE I. Initial and final values of the physical properties of the upper and lower mixed layers of the double-diffusive interface system during the July–August 2004 experiment.

Initial upper layer	Initial lower layer	Final
$T_I = 18.9\ °C$	$T_{II} = 26.7\ °C$	$T_I = T_{II} = 23.7\ °C$
$S_I = 2.2$ psu	$S_{II} = 13.5$ psu	$S_I = S_{II} = 8.3$ psu
$\rho_I = 1000.1\ kg/m^3$	$\rho_{II} = 1006.7\ kg/m^3$	$\rho_I = \rho_{II} = 1003.6\ kg/m^3$
$c_I = 1481.5$ m/s	$c_{II} = 1515.7$ m/s	$c_I = c_{II} = 1502.3$ m/s

PXI-5112) with custom-written LabView data acquisition software. The microstructure data were then filtered using a Butterworth filter with a 100-Hz cutoff. Profiles of temperature and conductivity were collected several times a day throughout the duration of the experiment. The interface thickness was determined from the conductivity profiles (as the conductivity sensor has a faster response time than the temperature sensor) by looking for rapid changes in the conductivity gradient (greater than a standard deviation of the mean mixed layer values). A small number of profiles had more noise than others, in which case the interface thickness was determined manually. Density and sound speed profiles were calculated from the temperature and conductivity profiles by matching the dynamic responses of the temperature and conductivity probes (Secs. 3c and 3d of Schmitt *et al.*, 2005). A total of 37 microstructure profiles were conducted during the July–August 2004 experiment (Fig. 4).

The DD interface was visibly disrupted by the passage of the microstructure instruments. The interface was allowed to settle for 15–20 min after each microstructure profile before any acoustic data were collected. The appropriate duration for the settling time was determined by monitoring the interface both acoustically (the interface disruption manifested itself as increased variability in the backscattered echoes from various instruments mounted along the side of the tank) and visually using the shadowgraph system.
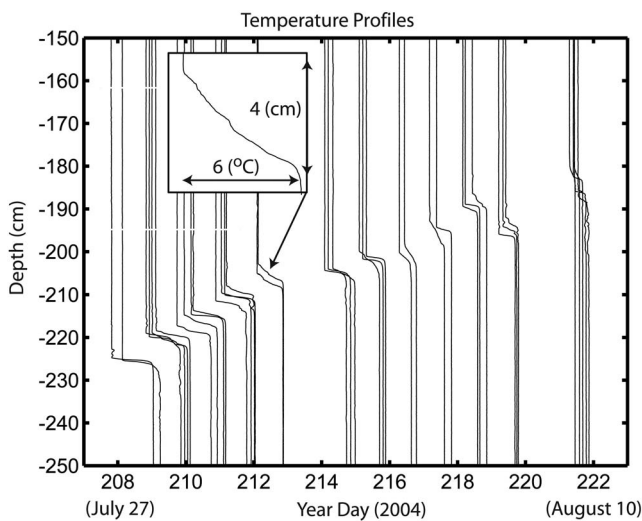

FIG. 4. Temperature profiles collected during the July–August 2004 experiment with the temperature microstructure sensors. The inset shows a close-up of the DD interface. The interface slowly migrated upwards, an effect that has been attributed to the nonlinearity of the equation of state (McDougall, 1981; Schmitt *et al.*, 2005).
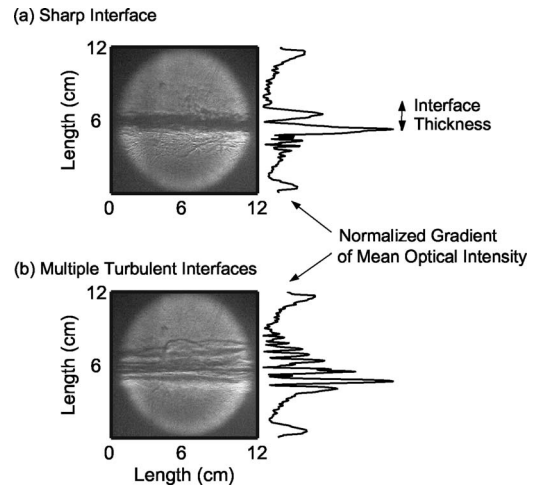

FIG. 5. Shadowgraph images collected on year day 214 (2 August), 2004: (a) A sharp double-diffusive interface and (b) a turbulent double-diffusive interface after the passage of an internal wave or seiche. The line plots to the right of the shadowgraph images show the normalized gradient of the mean optical intensity. The interface thickness for the sharp interfaces was calculated from the separation between the two primary peaks in the normalized gradient of the mean intensity.

The micro-temperature sensors were calibrated by the manufacturer various times throughout the experiments. The temperature was also verified by comparison with the fixed CT sensors in the upper and lower mixed layers. It was assumed that the response of the micro-conductivity sensor was linear and the fixed CT sensors in the upper and lower mixed layers provided a two-point calibration. The fixed CT sensors were calibrated by the manufacturer prior to installation and on two occasions in the DD interface tank by comparison to a calibrated CT instrument (Seabird SBE37).

D. Optical shadowgraph imaging

The optical shadowgraph system consisted of projecting a bright, collimated beam of monochromatic light horizontally through the DD interface, across the middle of the tank, and onto tracing paper, which was then imaged using a 5M pixel digital camera (Nikon Coolpix 5700). The light source was located near the bottom of the tank. The collimated beam was projected parallel to the tank, then reflected by a 45 deg mirror, and through two 40-cm-long rectangular windows of 1.27-cm-thick glass on diametrically opposite sides of the tank. The bottom sills of the shadowgraph windows were 230 cm below the top of the tank. Variations in temperature and salinity led to variations in the density and optical index of refraction within the interface, thus refracting light and allowing the interface to imaged (Williams, 1975). Optical shadowgraph images of the DD interface are inherently qualitative because the light beam is projected across the entire width of the tank, thus integrating horizontally over almost 1 m of the interface. One-minute digital movies of the shadowgraph imaged interface were collected periodically throughout the experiment, at a 15-Hz frame rate (900 images per minute-long movie).

Typical shadowgraph images of the DD interface exhibited two bright edges with an almost completely dark band in between [Fig. 5(a)]. The interface thickness was obtained by

TABLE II. Transducer and general experimental parameters. Unless otherwise stated, all parameters are evaluated at center frequency and at a range of $r_{scat}=75$ cm.

	250-kHz BB (200–300 kHz)	500-kHz BB (350–565 kHz)
Center frequency (kHz)	250	500
Transducer diameter, D (cm)	2.54	1.53
Full beamwidth, θ (degrees at −3 dB)	14.10	12.50
Directivity index (dB)	8.70	8.73
Far field, D^2/λ (cm)	10.75	6.82
First Fresnel radius, $\sqrt{\lambda r_{scat}}$ (cm)	4.75	3.35
Footprint radius, $r_{scat} \tan(\theta/2)$ (cm)	10.45	8.85
Pulse length, T (μs)	200	400 (300)
Bandwidth, B (kHz)	100	215
SNR gain, $2BT$	40	170 (130)
Inverse bandwidth, $1/B$ (μs)	10	4.65
Spatial resolution (cm): pulse compression	1.5	0.7
Spatial resolution (cm): pulse length	15	30(23)
No. of 1-Hz 30-min data acquisition periods	17	12
No. of 10-Hz 3-min data acquisition periods	17	NA

finding the separation between the two largest peaks in the gradient of the mean light intensity across each image [Fig. 5(a)]. The interface thickness was not calculated for images in which either the upper or lower edges of the dark band were not sufficiently distinct to give significant gradients above the background noise [Fig. 5(b)].

E. Acoustic scattering hardware and calibration

The acoustic scattering system, described below, consisted of a custom-built backscattering array, a programmable pulse-echo system, and custom-written data acquisition software.

1. Acoustic array and transducers

The acoustic backscattering array consisted of two pairs of identical transducers facing approximately vertically down. The transducers were mounted on two Plexiglas plates that could be rotated to focus the transducers at a particular range, that is, the orientation of each transducer relative to the horizontal (<5 degs to the horizontal at the ranges of this experiment) could be adjusted so that the acoustic footprint of each transducer pair was coincident at a particular range. Each pair of transducers, consisting of a transmitter and receiver, was as closely spaced as possible (7.5 cm center-to-center) to simulate backscattering. This configuration was chosen over a single transmit/receive transducer to minimize switching noise at close ranges. The transducers used were 250- and 500-kHz center frequency octave-bandwidth broadband (BB) (pistonlike) transducers (Table II). The transmitted signals were linearly modulated chirps with frequency sweeps from 200 to 300 kHz and from 350 to 650 kHz. In fact, for the 500-kHz BB transducers the usable band (−6 dB to −6 dB) was 350–565 kHz. The vertical position of the array in the tank could be adjusted in 1-mm increments spanning a 2.25-m range. The acoustic data presented here were collected at a range of $r_{scat}=75$ cm.

2. Pulse-echo system

The pulse-echo electronics (Fig. 6) was computerized and used for both the signal generation and digitization. The system consisted of a National Instruments (NI) data acquisition system (NI Model PXI-1000B) with an embedded computer controller (NI Model PXI-8175 running Windows 2000) and custom-written LabView data acquisition software. The transmitted signals were generated by a single-channel, 12-bit, 40 MHz Arbitrary Waveform Generator (NI Model PXI-5411), and then amplified by a 100-W linear power amplifier (ENI Model 2100L: 50-dB gain, 10-kHz to 12-MHz bandwidth). The received signal was amplified and filtered by an integrated preamplifier and bandpass filter (RITEC Inc., Model BR-640A: 32-dB gain, 100-kHz to 3-MHz bandwidth). A multi-channel high-speed (10 MHz per channel) simultaneously sampling DAQ module (NI
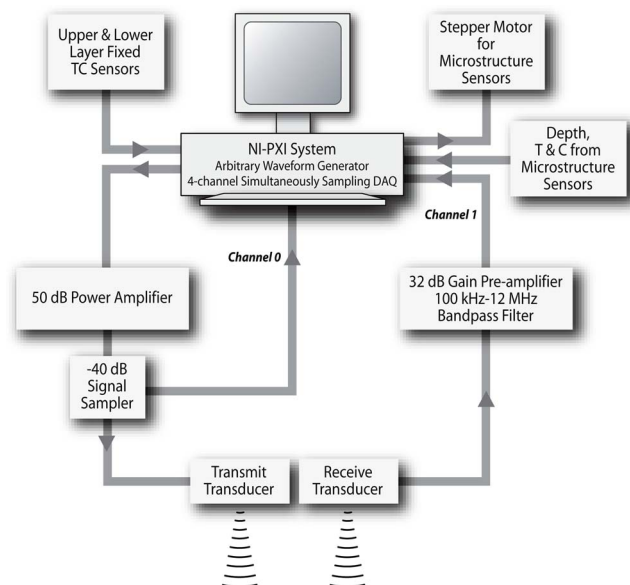

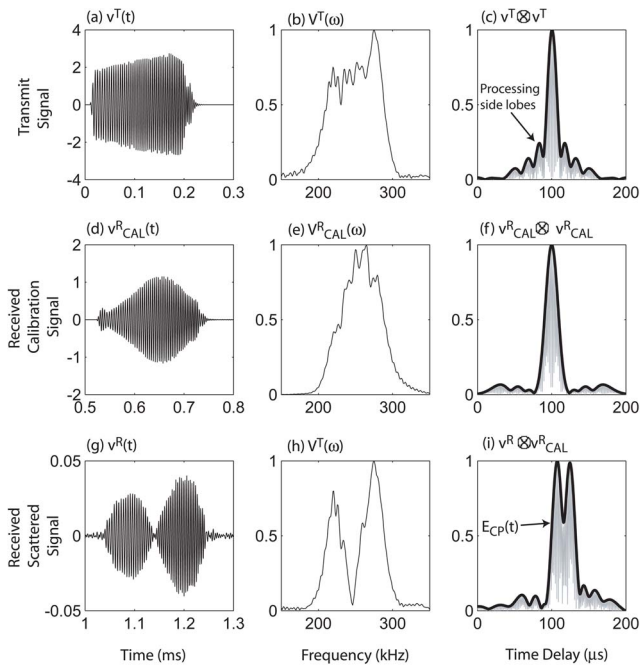FIG. 6. (Color online) Box diagram of the pulse-echo electronics used to perform the experiments.

FIG. 7. (Color online) Top row: (a) Typical transmit time series, $v^T(t)$, (b) the Fourier transform, $V^T(\omega)$, of the transmit time series, and (c) the normalized autocorrelation function of the transmit time series, $v^T(t) \otimes v^T(t)$, where $\otimes$ represents cross-correlation. Center row: (d) Typical received calibration time series, $v_{cal}^R(t)$, (e) the Fourier transform, $V_{cal}^R(\omega)$, of the received calibration time series, and (f) the normalized autocorrelation function of the received calibration time series, $v_{cal}^R(t) \otimes v_{cal}^R$. Bottom row: (g) Typical received time series of scattering from the DD interface, $v^R(t)$, (h) the Fourier transform, $V^T(\omega)$, of the received time series, and (i) the normalized compressed pulse output of the received time series, $v^R(t) \otimes v_{cal}^R$. The solid black lines in (c), (f), and (i) correspond to the envelope of the compressed pulse output, E_{CP}.

Model PXI-6115) made it possible to synchronously sample up to four input signals. All transmit and receive signals were sampled at 2 MHz for the July–August 2004 experiment. All the electronics and tank water were grounded to the same ground. Both the transmit voltage time series, $v^T(t)$, as measured by a 40-dB-down signal-sampler (RITEC Inc., Model SS-40) on the output end of the power amplifier, and received voltage time series, $v^R(t)$, were digitized during each ping (Fig. 7). A third-order Butterworth bandpass filter was applied to the received voltage time series, with cutoff frequencies at 150 and 350 kHz for the 250-kHz BB data, and at 300 and 700 kHz for the 500-kHz BB data. The echoes from the DD interface were range gated to eliminate any unwanted echoes. Acoustic data were collected for 30-min periods at a 1-Hz repetition rate (1800 pings per file) and for 3-min periods at a 10-Hz repetition rate (1800 pings per file), various times a day from the time the DD interface was generated to the time it became unstable and overturned (Table II).

3. Calibration of acoustic system

The technique used for the calibration measurements is similar in principle to a self-reciprocity calibration and involves separating the transducers so that they are directly facing each other. The transmitted, $v_{cal}^T(t)$, and received, $v_{cal}^R(t)$, calibration voltage time series are measured while

keeping all other system parameters identical to those for the backscattering measurements. However, the transmit amplitude was reduced by approximately a factor of 15 in order to prevent saturation of the receive transducer when the transducers were facing each other in calibration mode. This technique has been used successfully in previous laboratory scattering experiments (DiPerna and Stanton, 1991; Stanton *et al.*, 1998). The separation between the transducers during the calibration procedure was $r_{cal} = 76.4$ cm. The calibration measurements were performed with the transducers well within the upper mixed layer to ensure that there was no scattering due to temperature and salinity microstructure. This calibration technique results in an estimate of the relative pressure incident on the DD interface and allows the acoustic system to be calibrated without detailed knowledge of parameters such as the transmit source level and transducer sensitivities.

Standard target calibrations were also performed using a 20-mm tungsten carbide (6% cobalt) sphere (Foote and MacLennon, 1984). There was excellent agreement between the measured and calculated target strengths, with the deep nulls reproduced across the frequency bands of interest, with particularly good agreement for the 250-kHz BB data.

4. Noise threshold and background reverberation

All echoes from the DD interface that were smaller than a threshold value for noise were discarded. The procedure followed for setting a value for the noise threshold involved digitizing data for each insonification of the DD interface that included a period of time that did not contain any echoes from any of the auxiliary instruments mounted on the tank or from the DD interface. This window of data was used to set the noise threshold for each ping. To maximize the data quality, a conservative noise threshold was set, and it was required that the mean voltage of each echo from the DD interface be larger than the maximum noise value recorded for that particular insonification.

Scattering from the tank without the DD interface present was measured to ensure that there were no unwanted returns, for example from the surface or side-lobe reflections from the tank walls, in the range-gate window that was used when the DD interface was present. Coherent subtraction of unwanted reverberation could not be performed as it was not possible to measure the scattering from the tank without the DD interface present at the exact same ranges (within a fraction of the acoustic wavelength) used to perform the backscattering measurements. The reason for this was that the position of the interface was slowly, but continuously, changing, and so the position of the acoustic array was gradually changed throughout the experiment so that the range to the interface was always 75 cm.

F. Acoustic data analysis

The far-field scattered pressure for a single scattering realization from the DD interface is given by p_{scat} and can be expressed in terms of the spherically divergent incident sound field at the DD interface, $p_{inc} = P_0 r_0 e^{ikr_{scat}}/r_{scat}$, where k is the acoustic wavenumber ($k = 2\pi/\lambda$, where λ is the acous-

tic wavelength) and P_0 is the incident wave amplitude at a reference distance r_0. However, there is some uncertainty in the range dependence of p_{scat}. The problem of scattering of spherically diverging waves from rough surfaces has received much attention in the literature over the years (e.g., Eckart, 1953; Beckmann and Spizzichino, 1963; Horton *et al.*, 1967; Medwin and Novarini, 1981; Pace *et al.*, 1985). There are two limiting cases that can be considered. If the characteristic surface roughness, or root-mean-square (rms) surface height, h_{rms}, is small compared to the wavelength ($h_{rms} \ll \lambda$), then the interface will appear as an infinite, smooth interface. In this case, the well-known image solution can be arrived at by decomposing the incident spherically diverging wave into a sum of incident plane waves, resulting in a $1/2r_{scat}$ range dependence for the scattered pressure (Sec. 4.3 in Brekhovskikh and Lysanov, 2001). At the other extreme, if the interface roughness is larger than the wavelength ($h_{rms} > \lambda$), then the interface will appear to be a distribution of point scatterers and the scattered pressure will have an $1/r_{scat}^2$ range dependence.

As the range dependence of the scattered pressure from the DD interface is not known, scattering experiments were performed over a range of distances from the interface ($r_{scat} = 50$, 75, 100, and 125 m), with the maximum range dictated by the size of tank. However, this restricted range was not sufficient to allow the range dependence to be established above the strong variability that was observed in the scattering.

1. Spectral domain

As a consequence of the uncertainty in the range dependence of the scattering, the frequency dependence of the scattered pressure is presented using the following equation (modified form of Eq. (10) in DiPerna and Stanton, 1991):

$$\frac{P_{scat}}{P_{inc}} = G(\omega) \frac{V^R(\omega)}{V_{cal}^R(\omega)} \frac{r_{scat}}{r_{cal}}, \tag{1}$$

where ω is the angular frequency ($\omega = 2\pi c/\lambda$ and c is the speed of sound), P_{scat} is the amplitude of the scattered pressure, and P_{inc} is the amplitude of the pressure incident at the DD interface. $V^R(\omega)$ is the absolute value of the Fourier transform of the received voltage time series, and $V_{cal}^R(\omega)$ is the absolute value of the Fourier transform of the received calibration voltage time series. $G(\omega) = V_{cal}^T(\omega)/V^T(\omega)$ is the ratio of absolute value of the Fourier transform of the transmit calibration voltage time series to the absolute value of the Fourier transform of the transmit voltage time series. This slightly frequency-dependent factor accounts for the fact that the transmit amplitude during calibration was smaller than the transmit amplitude during the actual scattering experiments. This equation accounts for the spherical spreading of the wave incident on the DD interface and also for the spherical spreading of the calibration wave, but does not account for the range dependence of the wave scattered from the interface. Thus, P_{scat}/P_{inc} at one range cannot necessarily be compared directly to another range as there is an implicit range dependence still embedded in the equation. However, if the characteristic surface roughness of the DD

interface is small compared to the wavelength, and the scattered pressure has a $1/2r_{scat}$ range dependence, then P_{scat}/P_{inc} will be range independent. Losses due to attenuation are ignored in this analysis, which is a reasonable assumption given the short ranges used.

The high signal-to-noise (SNR) levels for the 250-kHz BB transducers allowed the spectral response of the echoes from the DD interface to be analyzed on a ping-by-ping basis in this frequency band throughout the duration of the July–August 2004 experiment. Low transducer sensitivity resulting in low SNR levels for the 500-kHz BB transducers precluded the analysis of the echoes in this frequency range towards the end of the experiment when the echoes from the DD interface were smaller as a result of the smaller temperature and salinity differentials across the interface.

2. Temporal domain: Pulse compression techniques

Increased signal-to-noise levels (proportional to $2BT$, where B is the bandwidth and T is the pulse length of the applied signal) and temporal resolution (proportional to $1/B$) can be achieved by applying pulse compression to the received voltage time series (Chu and Stanton, 1998). The compressed pulse output is given by cross-correlating the received voltage time series from the DD interface to the received calibration time series [Eq. (14) in Stanton *et al.*, 1998]:

$$CP(t) = k_{CP}^{-1} v^R(t) \otimes v_{cal}^R(t), \tag{2}$$

where $\otimes$ represents cross-correlation and k_{CP} is the autocorrelation function of v_{cal}^R evaluated at zero time lag. The envelope of the compressed pulse output is denoted $E_{CP}(t)$ (Fig. 7).

Peaks in the CP output corresponding to arrivals that are separated by greater than $1/B$ can be individually resolved. The interface thickness was calculated on a ping-by-ping basis for all broadband acoustic data that exhibited exactly two peaks in E_{CP}. The interface thickness is given by: $h = (c_I/2)|t_1 - t_2|$, where $t_i (i = 1, 2)$ are the delay times corresponding to the two peaks in E_{CP} and c_I is the sound speed in the upper mixed layer. All peaks in E_{CP} smaller than the signal processing side lobes of the autocorrelation function of v_{cal}^R, or smaller than 25% of the primary interface return, were discarded.

III. RESULTS

A. Individual echoes

The majority of the echoes from the DD interface did not exhibit significant spectral structure and had exactly one peak in the CP output. These "featureless" echoes were associated to larger mean scattering levels. However, a significant number of the echoes from the DD interface did show considerable spectral structure (Fig. 8). Many echoes exhibited a pattern in the spectral response that was consistent with the constructive and destructive interference pattern that would be expected from a layer with at least two primary interfaces, with nulls that were 10–15 dB below peak values
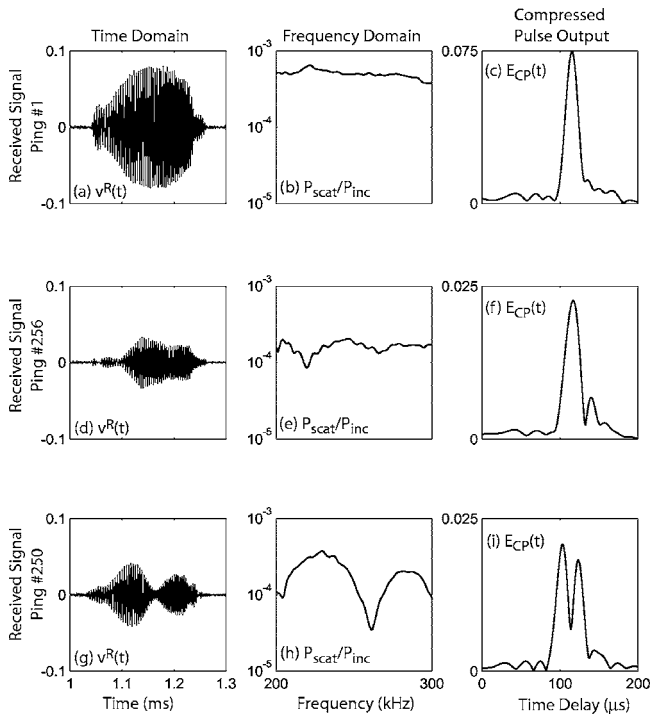
FIG. 8. Three typical received voltage time series in the 250-kHz BB frequency range on year day 214 (2 August), 2004. Ping 1 (top row) showing little spectral structure and a single peak in the CP output: (a) $v^R(t)$, (b) P_{scat}/P_{inc}, and (c) E_{CP}. Ping 256 (center row) showing little spectral structure but two peaks in the CP output: (d) $v^R(t)$, (e) P_{scat}/P_{inc}, and (f) E_{CP}. Ping 250 (bottom row) showing significant spectral structure and two peaks in the CP output: (g) $v^R(t)$, (h) P_{scat}/P_{inc}, and (i) E_{CP}.

FIG. 10. (a) P_{scat}/P_{inc}, (b) the envelope of the CP output, E_{CP}, as function of time and depth, and (c) the interface thickness inferred from echoes exhibiting exactly two peaks in the CP output, for the 30-min 250-kHz BB data (1800 pings at 1 Hz) followed by the 3-min 250-kHz BB data (1800 pings at 10 Hz) acquired on year day 214 (2 August), 2004. There was a 12-s delay separating the two data collection periods. Each ping in (b) has been normalized to its largest value.

for a given echo. For exactly two primary scattering interfaces, the nulls in the interference pattern occur when $\lambda(n+1/2)=h$ (for $n=0,1,2,\ldots$).

Pulse compression analysis of the echoes exhibiting significant spectral structure revealed that there were usually at least two clear peaks in the CP output. Due to the increased temporal resolution achieved through pulse compression, echoes that appeared relatively featureless in the frequency domain sometimes had separable peaks in the compressed pulse output (Fig. 8).

Based on the 30-min data acquisition periods, approximately 24% of the echoes from the DD interface in the 250-kHz BB frequency band showed exactly two peaks in the CP output, while approximately 31.5% of the echoes in the 500-kHz BB frequency band showed exactly two peaks in the CP output (Fig. 9). The number of echoes that had greater than
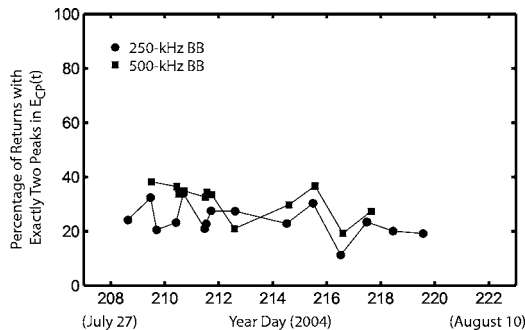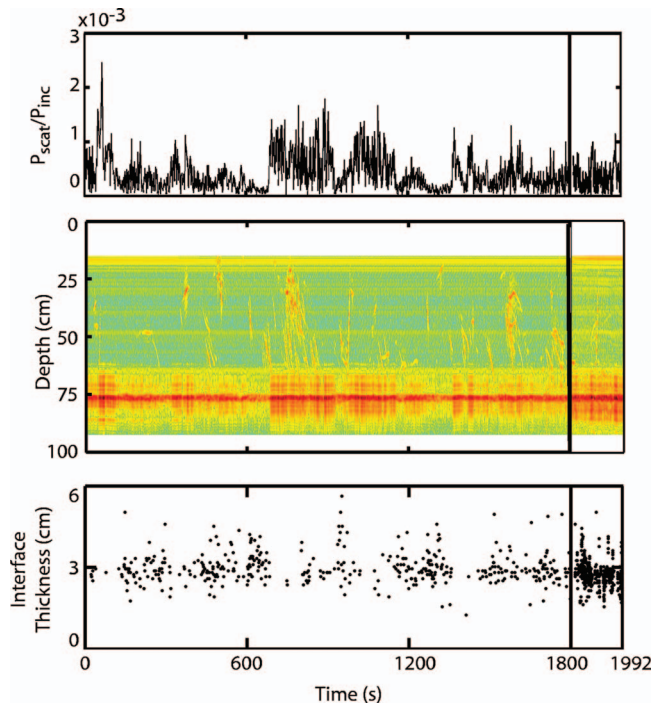
two peaks in the CP output in the 250-kHz BB frequency range was small, approximately 3% on the average, while the number of echoes that had more than two peaks in the CP output in the 500-kHz BB frequency range was larger, which is attributed in part to lower SNR in this frequency range. There was little correlation between the number of echoes that showed exactly two peaks in the CP output and the temperature (ΔT) or salinity (ΔS) differential between the upper and lower mixed layers.

The number of echoes showing exactly two peaks in the CP output based on the 3-min data acquisition periods was highly variable as intermittent high-scattering events (described in more detail in the next section), which are highly correlated to echoes that show little spectral structure, were not always fully captured in the 3-min data acquisition periods.

B. Variability of echoes

Significant ping-to-ping variability was observed for the echoes from the DD interface. For any given data acquisition period, the amplitude of the scattered pressure normalized by the incident pressure at the interface, P_{scat}/P_{inc}, fluctuated by more than an order of magnitude at all frequencies [Fig. 10(a)].

Intermittent events with scattering levels elevated by more than an order of magnitude occurred every few minutes. The duration of these intermittent events varied from tens of seconds to a couple of minutes. During these events, distinct returns could be seen in the water column above the
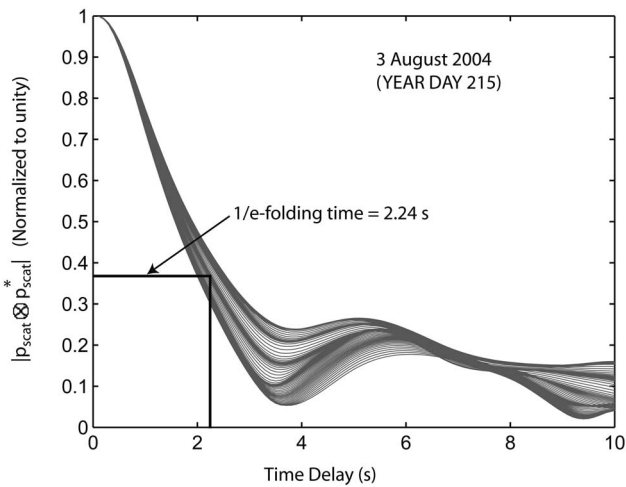

FIG. 9. Percentage of echoes with exactly two peaks in the CP output.

Lavery and Ross: Acoustic scattering from double-diffusive microstructure

FIG. 11. The amplitude of the autocorrelation function of the scattered pressure, $|p_{scat} \otimes p_{scat}^*|$, for all frequencies (in 1-kHz increments) for the 3-min, 10-Hz, 250-kHz BB data, collected on year day 215 (3 August), 2004. The e-folding time for these data is 2.24 s, representative of entire July–August 2004 experiment.

FIG. 12. Root-mean-square scattered pressure, $\langle (P_{scat}/P_{inc})^2 \rangle^{0.5}$, at 250 kHz for the 30-min 250-kHz BB data (solid circles) and at 500 kHz for the 30-min 500-kHz BB data (solid squares). The solid line, corresponding to the scale on the right-hand axis, shows the salinity contrast, ΔS, between the upper and lower mixed layers. The dashed line shows the reflection coefficient, arbitrarily scaled to fit the axes shown.

interface. These returns appeared to be due to physical structures that were generally moving upwards from the interface [Fig. 10(b)]. It is speculated that these structures are related to turbulent thermal plumes breaking away from the interface and traveling through the upper mixed layer, trapped by convection cells driven by the strong heating and cooling applied to the DD system. There were a larger number of echoes from the DD interface exhibiting either strong nulls in the frequency domain or multiple peaks in the CP output when the mean value of P_{scat}/P_{inc} across the frequency band was low and when less returns were observed in the water column above the interface.

The observed variability in the scattered echoes was related to the degree of heating and cooling applied to the DD system, which was held constant and high during the July–August 2004 experiment, but systematically modified in later experiments. When it was completely removed, the variability in the echoes quickly decreased, there were more echoes that had exactly two peaks in the CP output, and the mean scattered levels decreased. In addition, the scattering from physical structures above the DD interface disappeared.

C. Coherence of echoes

The temporal correlation between individual backscattered echoes (the decorrelation time scale) (Fig. 11) from the DD interface decreased significantly in approximately 2–3 s, due to changes in the position, thickness, and roughness of the DD interface resulting from processes such as waves on the interface and turbulent plumes. The decorrelation time scale was determined by calculating the amplitude of the autocorrelation of the scattered pressure, $|p_{scat} \otimes p_{scat}^*|$, at each frequency for all pings in a given data collection period. The 3-min data acquisition periods (10-Hz repetition rate) were used for this analysis to ensure that the shortest time scales were adequately sampled. However, the longer 30-min data collection periods we sampled sufficiently fast (1 Hz) that the Nyquist sampling criterion was satisfied. The decorrela-
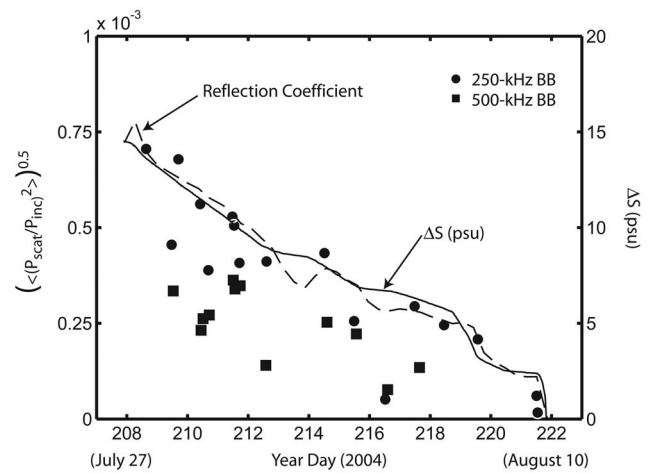
tion time scale was relatively uniform across all frequencies, and throughout the duration of the experiment. As a result of the short decorrelation time scale, over any given 30-min data collection period, the echoes from the DD interface were almost completely incoherent, that is $\langle p_{scat} \rangle^2 \approx 0$.

The decorrelation time scale is in good agreement with the time scale dictated by interface waves, in which the layer moves up and down, or oscillates, at the buoyancy frequency scaled appropriately for a DD interface (Turner, 1973):

$$N_{DD} = [(1 - 1/\text{Le})/3(\text{Pr} + 1)]^{1/2} N, \tag{3}$$

where N is the buoyancy frequency ($N^2 = -g/\rho \, \partial \rho / \partial z$ and g is the acceleration due to gravity), $\text{Le} = \kappa / \kappa_S (\approx 1.5)$ is the Lewis number (κ and κ_S are the molecular diffusivity of heat and salt, respectively), and $\text{Pr} = \nu / \kappa (\approx 6.32)$ is the Prandtl number (ν is the kinematic viscosity). For typical parameters of the DD interface experiment, $1/N_{DD} \approx 1/(1.55N) \approx 3$ s. It was not possible to probe the DD interface on relevant time scales using the direct microstructure sensors as the interface was significantly disturbed for 15–20 min after each of these measurements.

D. Dependence of echoes on the physical parameters controlling the double-diffusive interface

Over the duration of the experiment, the root-mean-square scattered pressure, $(P_{scat}/P_{inc})_{rms} = \langle (P_{scat}/P_{inc})^2 \rangle^{0.5}$, where the average is over all echoes from the DD interface in a 30-min data collection period, decreased as the temperature and salinity differentials across the DD interface decreased. The trend generally followed the trend observed in the salinity differential across the interface (ΔS) (Fig. 12) but not temperature differential (ΔT) (results not shown). Though this was generally also the case for the 3-min data collection periods, incomplete sampling of the strong but intermittent events resulted in significantly increased variability. The density contrast was more important than the sound speed contrast in determining the trend in root-mean-square scattered
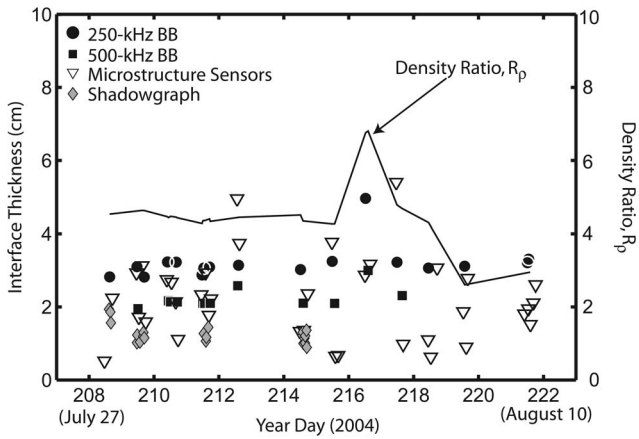
FIG. 13. Mean interface thickness based on the 30-min data acquisition periods for the 250-kHz BB (solid circles) and the 500-kHz BB (solid squares) acoustic data. The interface thickness was determined on a ping-by-ping basis from the separation between the peaks in the CP outputs that exhibited exactly two peaks, and then averaged over the 30-min data acquisition periods. The interface thickness as determined from the direct microstructure sensors (open triangles), and from 1-min averages of optical shadowgraph images (solid gray diamonds), are also shown.

pressure, which is not surprising as temperature plays a more important role than salinity in determining sound speed. The root-mean-square scattered pressure was slightly smaller in the 500-kHz BB frequency range than in the 250-kHz BB frequency range.

E. Interface thickness

The interface thickness was relatively uniform throughout the duration of the experiment (Fig. 13) until the DD system was close to overturning, independent of changes in the temperature and salinity differential across the DD interface. However, as the applied heating and cooling was maintained relatively constant throughout the experiment, the density ratio, R_ρ, which in later experiments was found to be important in controlling the interface thickness, was also relatively constant. R_ρ was briefly elevated above its nominal value of 4.5 on 4 August, and the interface thickness was seen to increase (Fig. 13). The acoustically inferred estimates of interface thickness based on the 500-kHz BB data were in better agreement with the direct micrsotructure and optical shadowgraph estimates, potentially due to the larger bandwidth and increased spatial resolution of the 500-kHz BB transducers.

IV. COMPARISON OF SCATTERING DATA WITH A SIMPLE MODEL

In this section, the scattered echoes from the double-diffusive interface are compared to a one-dimensional weak-scattering model that includes both the actual and idealized representations of the density and sound speed profiles [Fig. 14(a)]. This simple model consists of dividing the density and sound speed profiles into a finite number of sublayers, each with homogeneous density and sound speed (Gupta, 1966). The upper and lower mixed layers are modeled as homogeneous half-spaces. The scattered pressure at each interface is then calculated and added coherently. The scatter-
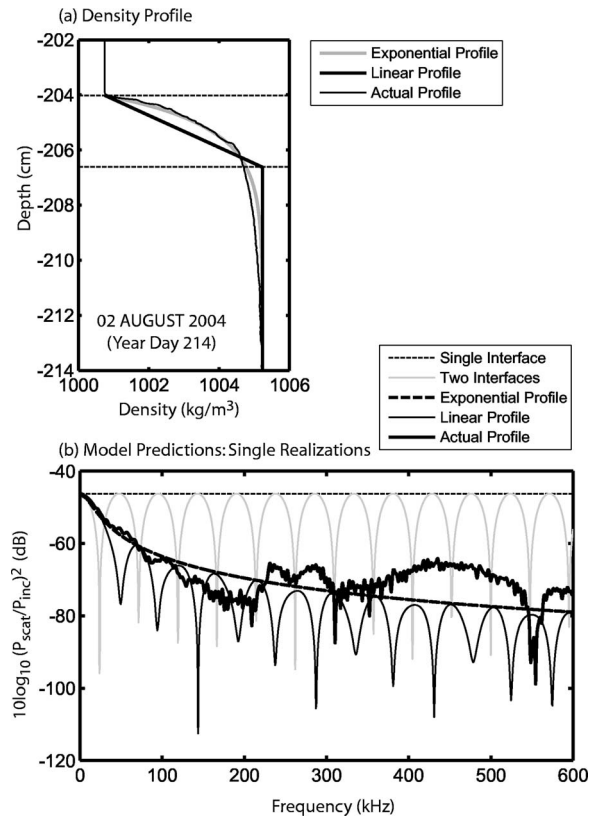

FIG. 14. (a) Measured density profile (thin black line) through the DD interface on year day 214 (2 August), 2004. The measured density profile was fit to a linear profile (thick black line) and an exponential profile (thick gray line). (b) Predicted scattering $10 \log_{10} (P_{\text{scat}}/P_{\text{inc}})^2$ versus frequency for a spherically diverging wave incident on the DD interface on year day 214 (2 August), 2004 assuming a single interface (thin dashed black line), a two-interface layer (thin gray line), exponential density and sound speed profiles (thick dashed black line), linear density and sound speed profiles (thin black line), and the actual density and sound speed profiles (thick black line).

ing from the DD interface falls into the weak-scattering regime as the density and sound speed contrasts across the interface, based on measurement of temperature and conductivity, were small (reflection coefficient $< 19.5 \times 10^{-3}$). Using this simple model, the scattered pressure can be calculated for both incident plane and spherical waves.

A. A one-dimensional weak-scattering model for the double-diffusive interface

1. Single interface

For an incident plane wave scattering from a single, infinite, smooth, interface, the magnitude of the scattered pressure normalized by the magnitude of the pressure incident at the interface is given by

$$\frac{P_{\text{scat}}}{P_{\text{inc}}^{PW}} = R_{I,II} = \frac{\rho_{II}c_{II} - \rho_I c_I}{\rho_{II}c_{II} + \rho_I c_I}, \tag{4}$$

where $P_{\text{inc}}^{PW} = P_0$ and $R_{I,II}$ is the traditional reflection coefficient. For a spherically spreading incident wave, the magnitude of the backscattered pressure is given by the image solution: $P_{\text{scat}} = R_{I,II} P_0 r_0/2r_{\text{scat}} = P_{\text{inc}} R_{I,II}/2$. However, this single-interface model cannot explain the echoes from the DD interface that exhibit constructive and destructive inter-

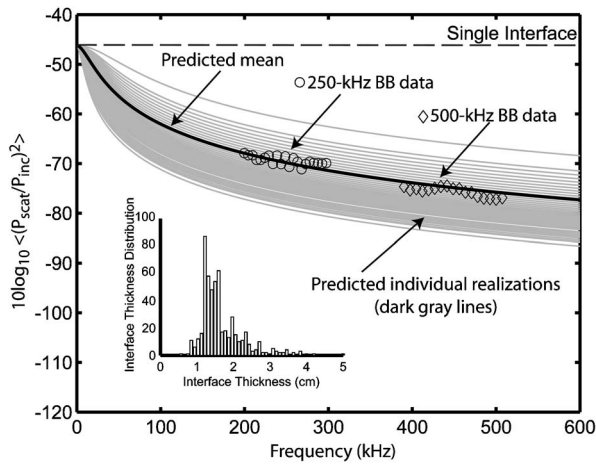Lavery and Ross: Acoustic scattering from double-diffusive microstructure

FIG. 15. Comparison of measured and predicted scattering using a one-dimensional weak-scattering model with no adjustable parameters for spherically diverging acoustic waves incident on the DD interface on year day 214 (2 August), 2004. The predicted scattering is based on exponential density and sound speed profiles and on the distribution of interface thicknesses acoustically inferred from the 500-kHz BB data (inset). The exponential decay parameters h_c and h_c were related to the acoustically derived interface thickness, h, by $h_c = 1.93h$ and $h_\rho = 2.3h$. Individual realizations are shown in light gray and the model average is shown in black. The symbols show the 30-min incoherently averaged data, $10 \log_{10} \langle (P_{scat}/P_{inc})^2 \rangle$, for the 250-kHz BB data (circles) and 500-kHz BB data (diamonds).

ference patterns (or multiple peaks in the CP output) and significantly overpredicts the observed scattering from the DD interface (Figs. 14 and 15).

2. Single homogeneous layer (two interfaces)

A model that consists of two, infinite, smooth interfaces separated by a homogenous fluid layer with intermediate properties between the upper and lower mixed layers can, in general terms, explain the echoes with exactly two peaks in the CP returns (Fig. 14). For an incident plane wave, the magnitude of the scattered pressure normalized by the magnitude of the pressure incident at the interface is given by (Sec. 3.3 in Brekhovskikh and Lysanov, 2001)

$$\frac{P_{scat}}{P_{inc}^{PW}} = \frac{R_{I,L} + R_{L,II}e^{2ik_L h}}{1 + R_{I,L}R_{L,II}e^{2ik_L h}}, \tag{5}$$

where k_L is the wavenumber within the homogeneous fluid layer, $R_{I,L}$ is the reflection coefficient between the upper mixed layer and the intermediate layer, $R_{L,II}$ is the reflection coefficient between the intermediate layer and the lower mixed layer, and h is the interface thickness. Since the scattering from each interface is weak, so that $R_{I,L} \ll 1$ and $R_{L,II} \ll 1$, and the transmission coefficient across each interface is approximately unity, then $P_{scat}/P_{inc}^{PW} \approx R_{I,L} + R_{L,II}e^{2ik_L h}$. This is the same expression that is obtained if only the first echo from each interface is coherently added.

Following similar arguments for an incident spherical wave, assuming weak scattering, the image solution at each interface, and coherently adding the first echo from each interface, the magnitude of the scattered pressure is given by

$$P_{scat} = P_0 r_0 \left(\frac{R_{I,L}}{2r_{scat}} + \frac{R_{L,II}}{2(r_{scat}+h)} e^{2ik_L h} \right). \tag{6}$$

The far-field approximation is valid since the interface thickness is much smaller than the range to the DD interface, thus $(r_{scat}+h) \approx r_{scat}$. Substituting $P_{inc} = P_0 r_0/r_{scat}$, the magnitude of the scattered pressure normalized by the magnitude of the pressure incident at the interface is given by

$$\frac{P_{scat}}{P_{inc}} \approx \frac{1}{2}(R_{I,L} + R_{L,II}e^{2ik_L h}). \tag{7}$$

Though this two-interface model can account for the constructive and destructive interference patterns of echoes from the DD interface with exactly two peaks in the CP output, it significantly overpredicts the observed scattering from the DD interface (Figs. 14 and 15).

3. Inhomogeneous multi-layered medium (multiple interfaces)

Following the procedure outlined above, the actual density and sound speed profiles can be used to calculate the scattering from the DD interface by dividing the profiles into N finely spaced homogenous sublayers of thickness Δ_n, where n runs from 1 to N. The thickness of each sublayer was set to be $\lambda_{600}/20$, where λ_{600} is the wavelength corresponding to the highest frequency of interest, namely 600 kHz. Assuming an incident spherical wave, weak scattering at each interface, the image solution at each interface, including only the first echo from each interface, and correctly accounting for the phase at each interface, then the magnitude of scattered pressure is approximately given by

$$P_{scat} \approx P_0 r_0 \left(\frac{R_{I,1}}{2r_{scat}} + \sum_{n=1}^{N} \frac{R_{n,n+1}e^{2i\sum_{m=1}^{n}k_m\Delta_m}}{2(r_{scat} + \sum_{m=1}^{n}\Delta_m)} \right), \tag{8}$$

where the reflection coefficient between each sublayer is given by $R_{n,n+1}$, $R_{I,1}$ is the reflection coefficient between the upper mixed layer and the first sublayer, and $R_{N,N+1} = R_{N,II}$. Again, the far-field approximation is valid since the interface thickness is much smaller than the range to the DD interface, thus $(r_{scat} + \sum_{m=1}^{N}\Delta_m) \approx r_{scat}$. The magnitude of the scattered pressure normalized by the magnitude of the pressure incident at the interface is given by

$$\frac{P_{scat}}{P_{inc}} \approx \frac{1}{2}\left(R_{I,1} + \sum_{n=1}^{N} R_{n,n+1}e^{2i\sum_{m=1}^{n}k_m\Delta_m} \right), \tag{9}$$

which is half the magnitude that would be obtained if the incident waves had been plane instead of spherical waves. The assumptions made in arriving at this expression are similar in principle to the assumptions of the distorted wave Born approximation, in which it is assumed that the incident wave is unaffected by the scattering from the preceding sublayers, but correctly accounts for the change in the phase of the incident wave as it traverses through each sublayer. This expression assumes normal incidence as the experiment was performed in the backscattering configuration. It is straightforward to generalize the formulation to other angles of incidence, at least for incident plane waves, by replacing k_n

with $k_n \cos \gamma_n$, where γ_n is the angle of incidence, measured from the normal, at the front interface of each sublayer, and γ_n is related to γ_{n+1} by Snell's law, namely $k_n \sin \gamma_n = k_{n+1} \sin \gamma_{n+1}$.

The reflection coefficient of a plane acoustic wave incident on an arbitrary number of layers, each of which has constant density and sound speed, but is not necessarily weakly scattering, can be easily calculated numerically (Sec. 3.3 in Brekhovskikh and Lysanov, 2001). The weak scattering assumption made here was tested against this numerical approach for actual density and sound speed profiles for incident plane waves. In addition, the reflection of a plane acoustic wave incident on a layered medium with density and sound speed that vary continuously with depth can be calculated analytically for a restricted number of idealized profiles (Robins, 1990, 1991). The accuracy of Eq. (9) was tested by comparison to a number of these analytical solutions.

B. Density and sound speed profiles

The scattering from the DD interface was calculated using Eq. (9) with the actual density and sound speed profiles as well with idealized profiles [Fig. 14(a)]. Idealized profiles provide insight into the important scattering processes as well as allowing predictions to be made when the actual density and sound speed profiles are not known. Exponential profiles are typically used by physical oceanographers to address the mismatch in the time response of microstructure temperature and conductivity sensors (Schmitt *et al.*, 2005). Thus, exponential density and sound speed profiles were used, given by

$$\rho(d) = \rho_I + (\rho_{II} - \rho_I)(1 - e^{-d/d_\rho}), \qquad (10)$$

$$c(d) = c_I + (c_{II} - c_I)(1 - e^{-d/d_c}), \qquad (11)$$

where d is the depth, $d=0$ is defined as the top of the interface, and the density and sound speed are set to ρ_I and c_I, respectively, for $d<0$. d_ρ and d_c are constants that determine how fast the profiles asymptote to the lower-layer homogeneous values of density (ρ_{II}) and sound speed (c_{II}). d_ρ and d_c were determined by performing a least-squares fit of the measured profiles to the predicted profiles, namely $\sum_{n=1}^{N}[\rho_{\text{measured}}(d_n) - \rho(d_n)]^2$ and $\sum_{n=1}^{N}[(c_{\text{measured}}(d_n) - c(d_n)]^2$ were minimized. Linear density and sound speed profiles were also used, given by

$$\rho(d) = \begin{cases} \rho_I + (\rho_{II} - \rho_I)d/h_\rho & \text{for } d < h_\rho, \\ \rho_{II} & \text{for } d \geq h_\rho, \end{cases} \qquad (12)$$

$$c(d) = \begin{cases} c_I + (c_{II} - c_I)d/h_c & \text{for } d < h_c, \\ c_{II} & \text{for } d \geq h_c. \end{cases} \qquad (13)$$

h_ρ and h_c were determined by performing a least-squares fit of the actual density and sound speed profiles to the linear profiles. As with the exponential profiles, $d=0$ is defined as the top of the interface, and the density and sound speed are set to ρ_I and c_I, respectively, for $d<0$. Only data for which $(c-c_I)/(c_{II}-c_I)$ and $(\rho-\rho_I)(\rho_{II}-\rho_I) < 0.95$ were included in the linear fits. The error in the least squares fit was smaller

when exponential profiles were used to represent the actual density and sound speed profiles rather than linear profiles. For the direct microstructure profiles of density and sound speed obtained on year day 214 (2 August), 2004 in between the 250- and 500-kHz BB data acquisition periods, it was found that $h_c = 1.93 d_c$ and $h_\rho = 2.3 d_\rho$.

C. Model predictions

Modeling the DD interface with linear density and sound speed gradients results in a constructive and destructive interference pattern, with the positions of the nulls dictated by the interface thickness. There is a significant phase-shift (almost completely out of phase) in the position of the nulls [Fig. 14(b)] relative to a single layer with two interfaces. The value of $P_{\text{scat}}/P_{\text{inc}}$ is similar to that of a single interface at low frequencies (long wavelengths relative to the interface thickness), however, the peak values are almost 25 dB smaller at the frequencies relevant to this study (200–600 kHz).

The constructive and destructive interference pattern is completely eliminated when the DD interface is modeled with exponential density and sound speed profiles [Fig. 14(b)]. $P_{\text{scat}}/P_{\text{inc}}$ is again approximately 25 dB smaller than a single sharp interface at the frequencies relevant to this study.

When the actual density and sound speed profiles are used to model the DD interface, the clear constructive and destructive interference pattern that is observed when the DD interface is modeled by linear sound speed and density profiles is significantly reduced, though there is increased fine-scale spectral structure. $P_{\text{scat}}/P_{\text{inc}}$ is again reduced by approximately 25 dB over the frequency range of interest, relative to a single interface [Fig. 14(b)].

D. Comparison of model predictions to data

It was not possible to perform coincident acoustic scattering and direct microstructure measurements of the DD interface. As a consequence it is not possible to compare scattered spectra on a ping-by-ping basis to predictions based on actual density and sound speed profiles. However, it is possible to compare the incoherently averaged echoes, $\langle (P_{\text{scat}}/P_{\text{inc}})^2 \rangle$, where the average is over all echoes in a 30-min data acquisition period, to model averages, where the averages are over the acoustically inferred distribution of interface thicknesses. This comparison is shown in Fig. 15 for the data collected on year day 214 (2 August), 2004. The acoustically inferred distribution of interface thicknesses based on the 500-kHz BB data was used as this agreed better than the inferences based on 250-kHz BB data with both the direct microstructure and optical shadowgraph estimates of the interface thickness performed on this day, and throughout the experiment (Fig. 13 and Table III). Both exponential and linear profiles in density and sound speed were used to perform the model averages. Averaging the model predictions based on the linear profiles resulted in the smoothing of the nulls and the predicted trend closely followed the averaged predictions based on the exponential profiles, but shifted down by approximately 4 dB (results not shown).

TABLE III. Mean interface thickness throughout the duration of the July–August 2004 experiment. Data from year day 216 (4 August) have not been included in this mean as the density ratio was elevated on this day.

Method of measurement	Mean interface thickness (cm)	Standard deviation (cm)
Acoustically inferred (250-kHz BB)	3.2	1.2
Acoustically inferred (500-kHz BB)	1.8	0.7
Direct microstructure	2.2	1.1
Optically inferred	1.3	0.4

The remarkable agreement between the averaged model prediction, which contains no adjustable parameters, and the incoherently averaged broadband data strongly suggests that the range dependence of the scattered pressure is $1/2r_{scat}$, as this is an inherent assumption of the model.

E. Considerations for further modeling

The simple one-dimensional weak-scattering model developed here includes two important components of the problem of scattering of acoustic waves from DD interfaces, that is, incident spherical waves and gradients in the density and sound speed profiles. However, to more accurately model the scattering, both volume and surface roughness effects (Ivakin, 1997) should be included, for which knowledge of both the acoustic sampling volume (Foote, 1991) and the interface roughness is necessary.

Another important modeling consideration is the effect of small beamwidth transducers, resulting in an insonified area that is range dependent and only includes a finite number of Fresnel zones (Horton and Melton, 1970). The simple model described above assumes that an infinite number of Fresnel zones contribute to the scattering, while in fact the measurements are in the transition region with 2.5 to 6 Fresnel zones encompassed by the insonified region, depending on the frequency and transducer pair employed (Table II). To incorporate these effects, one approach is to decompose the incident spherical waves into a sum of incident plane waves (Sec. 4.3 in Brekhovskikh and Lysanov, 2001) before integrating over the size of the acoustic footprint at the DD interface. The importance of the size of the acoustic footprint relative to the size of the Fresnel zones could be investigated experimentally by performing scattering measurements with transducers operating in the same frequency band but with different beamwidths.

V. SUMMARY AND CONCLUSIONS

In this study, controlled laboratory measurements of high-frequency broadband acoustic backscattering from the diffusive regime of double-diffusive microstructure have been performed. The diffusive regime of double-diffusive microstructure is characterized by sharp density and sound speed interfaces. Acoustic backscattering has been measured for a range of physical parameters driving the double-diffusive microstructure. It has been demonstrated that double-diffusive microstructure can be investigated acousti-

cally on spatial and temporal scales that are difficult to achieve using techniques that are more commonly used to study oceanic microstructure, namely, free-falling direct microstructure sensors and optical shadowgraph techniques. The acoustic echoes from the double-diffusive interface have been analyzed in both the frequency domain, providing information on the spectral response of the scattering, and in the time domain, through pulse compression techniques that result in improved spatial resolution and increased signal-to-noise ratios. Exploiting broadband pulse compression techniques, the interface thickness has been remotely measured and found to be in reasonable agreement with the almost-coincident optical and direct microstructure measurements of interface thickness (Table III).

A simple one-dimensional weak-scattering model for spherically diverging acoustic waves incident on the double-diffusive interface, which includes realistic representations of the measured density and sound speed profiles, has been developed. Predictions based on this model, which has no adjustable parameters, are in significantly better agreement with the measured scattering than predictions based on a one-layer model in which the scattering is due to two smooth interfaces separated by a homogeneous, weakly scattering, fluid layer. Over the frequency range of interest, inclusion of the actual density and sound speed profiles decreases the predicted scattering by approximately 25 dB compared to a one-layer scattering model. The model developed here has illustrated that the scattering from the double-diffusive interface is sensitive to both the interface thickness and the exact shape of the density and sound speed profiles, for individual realizations.

A remote-sensing technique that could be used to map the extent of oceanic double diffusion, the evolution of multiple double-diffusive layers, and the thickness of such layers could lead to an increased understanding of the importance of double diffusion to oceanic mixing. However, it is unclear from the results of this study if the measurements of broadband acoustic scattering from laboratory generated double-diffusive microstructure can be extended to realistic oceanic double diffusion. Though the density ratio used in this study is typical of that found in oceanic double diffusion (almost by definition), the temperature and salinity gradients in the laboratory are significantly larger than those seen in typical oceanic double-diffusive thermohaline staircases. Thus, though the measurements performed in this study show promise, further work is needed to determine if high-frequency broadband acoustic scattering techniques are a viable remote sensing tool for studying the diffusive regime of oceanic double diffusion.

Beckmann, P., and Spizzichino, A. (**1963**). *The Scattering of Electromagnetic Waves from Rough Surfaces* (MacMillan, New York).

Brekhovskikh, L. M., and Lysanov, Y. P. (**2001**). *Fundamentals of Ocean Acoustics*, AIP Series in Modern Acoustics and Signal Processing (AIP, Springer-Verlag, New York).

Chu, D., and Stanton, T. K. (**1998**). "Application of pulse compression techniques to broadband acoustic scattering by live individual zooplankton," J. Acoust. Soc. Am. **104**, 39–55.

DiPerna, D. T., and Stanton, T. K. (**1991**). "Fresnel zone effects in the scattering of sound by cylinders of various lengths," J. Acoust. Soc. Am. **90**, 3348–3355.

Eckart, C. (**1953**). "The scattering of sound from the sea surface," J. Acoust. Soc. Am. **25**, 566–570.

Farmer, D. M., and Armi, L. (**1999**). "Stratified flow over topography: the role of small scale entrainment and mixing in flow establishment," Proc. R. Soc. London, Ser. A **455**, 3221–3258.

Fofonoff, P., and Millard, R. C., Jr. (**1983**). "Algorithms for computation of fundamental properties of seawater, 1983," UNESCO Tech. Pap. in Mar. Sci. **44**, 53.

Foote, K. G. (**1991**). "Acoustic sampling volume," J. Acoust. Soc. Am. **90**, 959–964.

Foote, K. G., and MacLennan, D. N. (**1984**). "Comparison of copper and tungsten carbiude calibration spheres," J. Acoust. Soc. Am. **75**, 612–616.

Goodman, L. (**1990**). "Acoustic scattering from oceanic microstructure," J. Geophys. Res. **95**, 11557–11573.

Goodman, L., Oeschger, J., and Szargowicz, D. (**1992**). "Ocean acoustics turbulence study: acoustic scattering from an axisymmetric plume," J. Acoust. Soc. Am. **91**, 3212–3227.

Gupta, R. N. (**1966**). "Reflection of sound waves from transition layers," J. Acoust. Soc. Am. **39**, 255–260.

Holbrook, S. W., Paramo, P., Pearse, S., and Schmitt, R. W. (**2003**). "Thermohaline fine structure in an oceanographic front from seismic reflection profiling," Science **301**, 821–824.

Horton, C. W., Mitchell, S. K., and Barnard, G. R. (**1967**). "Model studies of the scattering of acoustic waves from a rough surface," J. Acoust. Soc. Am. **41**, 635–643.

Horton, C. W., and Melton, D. R. (**1970**). "Importance of the Fresnel correction in scattering from a rough surface. II. Scattering coefficient," J. Acoust. Soc. Am. **47**, 299–303.

Ivakin, A. N. (**1997**). "A unified approach to volume and roughness scattering," J. Acoust. Soc. Am. **103**, 827–837.

Kelley, D. E., Fernando, H. J. S., Gargett, A. E., Tanny, J., and Ozsoy, E. (**2003**). "The diffusive regime of double-diffusive convection," Prog. Oceanogr. **56**, 461–481.

Lavery, A. C., Schmitt, R. W., and Stanton, T. K. (**2003**). "High-frequency acoustic scattering from turbulent oceanic microstructure: the importance of density fluctuations," J. Acoust. Soc. Am. **114**, 2685–2697.

Lavery, A. C., Wiebe, P. H., Stanton, T. K., Lawson, G. L., Benfield, M. C., and Copley, N. (**2007**). "Determining dominant scatterers of sound in mixed zooplankton populations," J. Acoust. Soc. Am. (accepted).

McDougall, T. J. (**1981**). "Double-diffusive convection with a nonlinear equation of state. II. Laboratory experiments and their interpretation," Prog. Oceanogr. **10**, 91–121.

Medwin, H., and Novarini, J. C. (**1981**). "Backscattering strength and the range dependence of sound scattered from the ocean surface," J. Acoust. Soc. Am. **69**, 108–111.

Mellberg, L. E., Johannessen, O. M., and Lee, O. S. (**1974**). "Acoustic effect caused by a deep thermohaline stepped structure in the Mediterranean Sea," J. Acoust. Soc. Am. **55**, 1081–1083.

Mellberg, L. E., and Johannessen, O. M. (**1972**). "Layered oceanic microstructure—it's effect on sound propagation," J. Acoust. Soc. Am. **53**, 571–580.

Moum, J. N., Farmer, D. M., Smyth, W. D., Armi, L., and Vagle, S. (**2003**). "Structure and generation of turbulence at interfaces strained by internal solitary waves propagating shoreward over the continental shelf," J. Phys. Oceanogr. **33**, 2093–2112.

Muench, R. D., Fernando, H. J. S., and Stegen, G. R. (**1990**). "Temperature and salinity staircases in the northwestern Weddell sea," J. Phys. Oceanogr. **20**, 295–306.

Neal, V. T., Neshyba, S., and Denner, W. (**1969**). "Thermal stratification in the Arctic Ocean," Science **166**, 373–374.

Oeschger, J., and Goodman, L. (**1996**). "Acoustic scattering from a thermally driven buoyant plume," J. Acoust. Soc. Am. **100**, 1451–1462.

Oeschger, J., and Goodman, L. (**2003**). "Acoustic scattering from a thermally driven buoyant plume revisited," J. Acoust. Soc. Am. **100**, 1451–1462.

Pace, N. G., Al-Hamdani, Z. K. S., and Thorne, P. D. (**1985**). "The range dependence of normal incidence acoustic backscatter from a rough interface," J. Acoust. Soc. Am. **77**, 101–112.

Proni, J. R., and Apel, J. R. (**1975**). "On the use of high-frequency acoustics for the study of internal waves and microstructure," J. Geophys. Res. **80**, 1147–1151.

Robins, A. J. (**1990**). "Reflection of plane acoustic waves from a layer of varying density." J. Acoust. Soc. Am. **89**, 1546–1552.

Robins, A. J. (**1991**). "Reflection of a plane wave from a fluid layer with continuously varying density and sound speed." J. Acoust. Soc. Am. **89**, 1686–1696.

Ross, T., and Lueck, R. (**2003**). "Sound scattering from oceanic turbulence," Geophys. Res. Lett. **30**, 1344.

Schmitt, R. W., Millard, R. C., Toole, J. M., and Wellwood, W. D. (**2005**). "A doubly-diffusive interface tank for dynamic-response studies," J. Mar. Res. **63**, 263–289.

Schmitt, R. W. (**1994**). "Double diffusion in oceanography," Annu. Rev. Fluid Mech. **26**, 255–285.

Seim, H. E., Gregg, M. C., and Miyamoto, R. T. (**1995**). "Acoustic backscatter from turbulent microstructure," J. Atmos. Ocean. Technol. **12**, 367–380.

Seim, H. E. (**1999**). "Acoustic backscatter from salinity microstructure," J. Atmos. Ocean. Technol. **16**, 1491–1498.

Stanton, T. K., Chu, D., Wiebe, P. H., Martin, L. V., and Eastwood, R. L. (**1998**). "Sound scattering by several zooplankton groups. I. Experimental determination of dominant scattering mechanisms," J. Acoust. Soc. Am. **103**, 225–235.

Stanton, T. K., Wiebe, P. H., Chu, D., and Goodman, L. (**1994**). "Acoustic characterization and discrimination of marine zooplankton and turbulence," ICES J. Mar. Sci. **51**, 469–479.

Turner, J. S. (**1973**). *Buoyancy Effects in Fluids* (Cambridge Univ. Press, Cambridge, UK).

Warren, J. D., Stanton, T. K., Wiebe, P. H., and Seim, H. E. (**2003**). "Inference of biological and physical parameters in an internal wave using multiple-frequency acoustic scattering data," ICES J. Mar. Sci. **60**, 1033–1046.

Williams, A. J. (**1975**). "Images of ocean microstructure," Deep-Sea Res. **22**, 811–829.